Laboratory data linking the reconfiguration of and drag on individual plants to the velocity structure and wave dissipation over a meadow of salt marshes under waves with and without current

Xiaoxia Zhang[1*], Heidi Nepf[2]

[1]Water Science and Environmental Engineering Research Center, College of Chemical and Environmental Engineering, Shenzhen University, Shenzhen, 518060, China

[2]Department of Civil and Environmental Engineering, Massachusetts Institute of Technology, Cambridge, Massachusetts, 02139, USA

Correspondence: Xiaoxia Zhang (xiaoxiazhang@szu.edu.cn)

Abstract

Salt marshes provide valuable ecosystem services, which are influenced by their interaction with current and waves. On the one hand, current and waves exert hydrodynamic force on salt marsh plants, which shapes the distribution of species within the marsh. On the other hand, the resistance produced by the plants can shape the flow structure, turbulent intensity, and the wave dissipation over the canopy. Because marsh plants are flexible structures, their reconfiguration modifies the drag felt by the plants and the flow. While several previous studies have considered the flexibility of the stem, few studies have considered the leaf component, which has been shown to contribute the majority of plant resistance. This paper reports a unique dataset that includes laboratory measurements of both the force on an individual plant and the flow structure and wave energy dissipation over a meadow of plants. In the individual plant experiment, the motion of the plant and plant drag, free surface displacement and velocity profile were measured. The individual plant experiments considered both a live marsh plant (*Spartina alterniflora*) and a mimic consisting of ten leaves attached to a central stem. For the meadow experiment, velocity profiles were measured both upstream and within the meadow, and free surface displacement was measured along the model marsh plant meadow with high spatial and temporal resolution. These experiments used five water depths (covering both submerged and emergent conditions), three wave periods (from long wave to short waves), seven wave heights (from linear to nonlinear waves), six current conditions (including pure current, pure wave, and combined current and waves). In summary, there are 102 individual plant tests and 58 meadow tests. The drag, free surface displacement, and velocity are reported in SMCW.mat file including the raw data, the phase average, and statistic values. The link to the plant motion videos is also provided. This dataset provides high quality measurements that can be used to develop and validate models of plant motion, hydrodynamic drag on individual plants, vegetation-generated turbulence, the evolution of flow structure through a meadow, and the transformation and dissipation of waves over natural salt marshes. The dataset is available from figshare with detailed instructions for reuse (https://doi.org/10.6084/m9.figshare.24117144; Zhang and Nepf, 2023a).

Keywords: salt marsh; flexible plant; drag force; reconfiguration; flow structure; wave dissipation;

1. Introduction

Salt marshes are a common feature of coastal and estuary regions, serving as important habitats and food sources for intertidal invertebrates and small fish (Boesch and Turner, 1984; Barbier et al., 2011). These marshes also play a crucial role in carbon sequestration, accumulating carbon stocks at a rate of 210 g/cm^2/year, the highest among all ecosystems on Earth (Pidgeon, 2009). Additionally, salt marshes provide shoreline protection by dissipating extreme waves (Zhang et al., 2020; Garzon et al., 2019b) and reducing erosion and enhancing sedimentation (Schoutens et al., 2019; Elschot et al., 2013; Huai et al., 2021). The health and function of salt marsh ecosystems depend on the interaction between the marsh and surrounding currents and waves. Currents and waves exert hydrodynamic forces on marsh plants, influencing the distribution of species within the marsh (Schoutens et al., 2022, 2020). In addition, because marsh plants are flexible, they reconfigure under hydrodynamic forces, modifying the forces experienced by the plants (Zhang and Nepf, 2021b), and the impact of plant resistance on flow structure (Chen et al., 2013; Lowe et al., 2005; Zeller et al., 2015; Lei and Nepf, 2021), turbulence intensity (Xu and Nepf, 2020), and wave energy transformation (Hu et al., 2014; van Veelen et al., 2020; Vuik et al., 2016).

Theories that quantify the hydrodynamic force on rigid cylinders and flat plates were developed in the 1950's (Morison et al., 1950; Keulegan and Carpenter, 1958). However, real plants are flexible and reconfigure under the influence of currents and waves, reducing the hydrodynamic forces they experience (Luhar and Nepf, 2011; Gosselin et al., 2010; Mullarney and Henderson, 2010; Zhu et al., 2020). Models have been developed to predict the forces on flexible structures by considering the reconfiguration and relative motion between the fluid and the plant (Luhar and Nepf, 2011; Mullarney and Henderson, 2010; Gosselin et al., 2010; Lei and Nepf, 2019b). Laboratory measurements have shown that real plants with different morphologies followed different scaling laws (Harder et al., 2004; Schutten and Davy, 2000; Jalonen and Järvelä, 2013; Whittaker et al., 2013; Zhang and Nepf, 2020). Many salt marsh plants consist of multiple flexible leaves attached to single, less flexible central stem, e.g., *Phragmites australis*, *Scirpus maritimus*, *Spartina alterniflora*, and *Spartina anglica*. For such plant, Zhang and Nepf (2021b) demonstrated that the force acting on a full model plant can be estimated by summing the forces on all the leaves and the stem, while applying a sheltering coefficient to account for the plant drag reduction due to the interaction and sheltering among the leaves and the stem. The sheltering

67 coefficient depends on the geometrical properties of the plant (mainly the distribution of leaves on
68 the stem) and does not vary with flow conditions. Based on this, predictive models were proposed
69 to estimate the forces acting on salt marsh plants with both leaves and stem (Zhang and Nepf,
70 2021b, 2022).

71 Within a canopy, the presence of plants can significantly alter the flow structure (Chen et al.,
72 2013; Lowe et al., 2005; Zeller et al., 2015; Lei and Nepf, 2021) and turbulence intensity (Xu and
73 Nepf, 2020), and reduce wave energy (Garzon et al., 2019a; Zhang et al., 2020; Maza et al., 2015).
74 The fully developed flow structure within a canopy has been extensively studied under both current
75 (Chen et al., 2013; Lei and Nepf, 2021) and wave conditions (Lowe et al., 2005) for both emergent
76 and submerged canopies. Specifically, the mean flow is determined by the distribution of the plant
77 frontal area for emergent canopies, and by the canopy drag and the ratio of water depth to plant
78 height for submerged canopies (Nepf, 2012). The wave orbital velocity experiences less
79 modification by a canopy due to the greater inertial force under waves compared to current (Lowe
80 et al., 2005), which allows the flow to penetrate deeper into the lower canopy region. The presence
81 of plants affects turbulence intensity directly through form drag and wake generated by plant
82 elements, and indirectly by adjusting the flow structure to create a greater shear and thus shear
83 production (Nepf, 2012). The resistance of plants can reduce wave height by 30% to 90% over the
84 first 30 m of a salt marsh (Ysebaert et al., 2011; Knutson et al., 1982; Zhang et al., 2020; Garzon
85 et al., 2019a), depending on the plant properties (density, geometrical, and mechanical
86 characteristics) and flow conditions (water depth, wave period, wave amplitude, with or without
87 current). Recent studies proposed simple predictions for the wave decay over salt marshes under
88 pure waves (Zhang et al., 2021, 2022), which has been extended to combined current and wave
89 conditions using the in-canopy total velocity (Zhang and Nepf, 2021a). However, a well-validated
90 theoretical model for the time-varying total velocity is currently lacking for salt marshes under
91 combined current and waves, which hinders the development of accurate models for canopy
92 turbulence and wave dissipation.

93 This paper presents both force measurements on individual salt marsh plants (Zhang and
94 Nepf, 2021b, 2022) and measurements of flow structure and wave decay along a meadow of salt
95 marsh plants (Zhang et al., 2021, 2022; Zhang and Nepf, 2021a). The experiments utilized model
96 plants that consisted of multiple flexible leaves attached to a central stem, which were designed to
97 be geometrically and dynamically similar to *Spartina alterniflora*, a common salt marsh species.

98   The test conditions varied from submerge to emergent, long wave to short waves, and linear to
99   nonlinear waves with and without following currents. In total, 102 individual plant tests and 58
100   meadow tests were conducted. The individual plant experiments (IE) provide synchronized
101   measurements of plant drag and free surface displacement, as well as 3-dimensional velocity
102   profiles provided as raw data, phase-averaged data, and statistical data. Additionally, link to videos
103   capturing the motion of the plants are provided. The meadow experiments (ME) provide time-
104   varying measurements of free surface displacement along the meadow at 10 and 15 cm intervals,
105   as well as velocity profiles upstream of and within the meadow with 1 to 2 cm vertical resolution.
106   This dataset can facilitate the development and validation of dynamic marsh plant models, enhance
107   predictions of marsh plant drag, and deepen our understanding of vegetation-induced turbulence,
108   the evolution of flow structure within a canopy, and the transformation and dissipation of waves
109   in natural salt marshes.
110

2. Method

112   The experiments were conducted in the Nepf Fluid Mechanics lab at MIT in a 24-m-long, 38-
113   cm-wide, 60-cm-tall water channel (Fig. 1). Monochromatic waves were generated with a piston-
114   type wavemaker. A beach with 1:5 slope and covered with a layer of 10-cm thick coconut fiber
115   was located at the downstream end of the channel, which limited the wave reflection to 7% ± 3%
116   for the tested conditions. Following currents (current and waves propagate in the same direction)
117   were generated by a variable speed pump. Two bricks elevated the beach by 9 cm above the bed
118   to allow the current to pass.
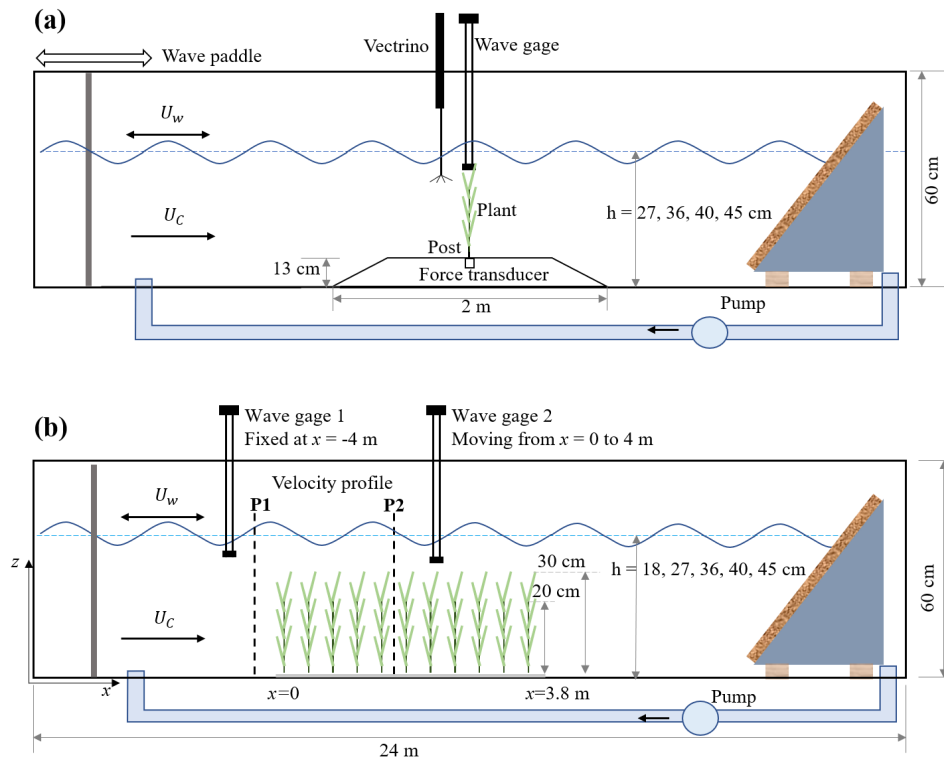
Fig. 1 Schematic of (a) the individual plant experiment (IE) and (b) the meadow experiment (ME), not to scale. The wave paddle and current inlet are at the left, and the wave-absorbing beach at the right. In subplot (a), the model plant was attached to a submersible force sensor housed in a 13-cm high acrylic ramp. A wave gage recorded the free surface displacement at the same longitudinal position as the plant, but 9 cm to the side. A Nortek Vectrino+ measured velocity 10-cm upstream of the plant position, but with the plant removed. In subplot (b), the model meadow was 3.8 m long and located at mid-length along the flume. Two wave gages measured the wave height at a stationary reference position (wave gage 1) and at multiple positions along the meadow (wave gage 2). Velocity in front (P1) and inside the meadow (P2) was measured by Vectrino+.
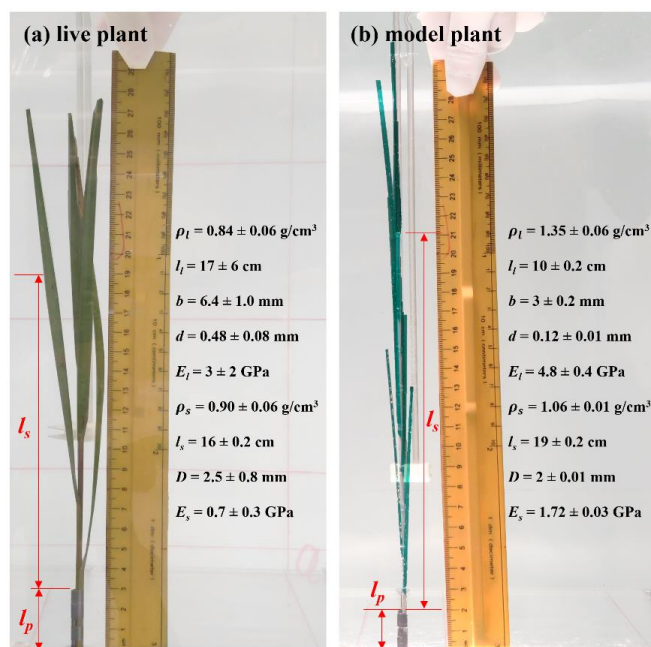
2.1 Individual plant experiment setup

The individual plant experiments (IE) tested a live *Spartina alterniflora*, a single flat plastic leaf, a single cylindrical stem, and a full model marsh plant consisting of 10 leaves attached to a central stem. These tests are labeled as live, leaf, stem, and model, respectively. Fig. 2 shows the

134   live and model plants with the corresponding plant properties (see also Figure 2 and Table 1 in

135   Zhang and Nepf, 2021). The live plant consisted of 5 leaves, the dimensions shown in Fig. 2a are

136   the mean ± SD of these leaves. The plant was attached to a stainless steel post with 2 mm diameter.

137   The length of the post above the ramp was l_p = 3, 4.5, 2, and 2 cm for the live, leaf, stem, and

138   model plant, respectively. The lower part of the post was attached to a submersible force sensor

139   (Futek LSB210 100g), which was mounted beneath an acrylic ramp (1-m top length, 2-m bottom

140   length, 13-cm height, and spanning the flume width, see Fig. 1a) to avoid interaction between fluid

141   motion and the sensor. IE measured the hydrodynamic force exerted on the plant, the motion of

142   the plant, and the associated hydrodynamic conditions (velocity profile and wave height). The

143   wave gauge was mounted at the same longitudinal position as the plant, but 9 cm to the lateral side.

144   Note that for each plant and each water depth, the zero position of the wave gauge and force sensor

145   was determined for still water, i.e., before the wave generator and current pump were turned on.

146

(a) live plant

$\rho_l = 0.84 \pm 0.06$ g/cm³

$l_l = 17 \pm 6$ cm

$b = 6.4 \pm 1.0$ mm

$d = 0.48 \pm 0.08$ mm

$E_l = 3 \pm 2$ GPa

$\rho_s = 0.90 \pm 0.06$ g/cm³

$l_s = 16 \pm 0.2$ cm

$D = 2.5 \pm 0.8$ mm

$E_s = 0.7 \pm 0.3$ GPa

(b) model plant

$\rho_l = 1.35 \pm 0.06$ g/cm³

$l_l = 10 \pm 0.2$ cm

$b = 3 \pm 0.2$ mm

$d = 0.12 \pm 0.01$ mm

$E_l = 4.8 \pm 0.4$ GPa

$\rho_s = 1.06 \pm 0.01$ g/cm³

$l_s = 19 \pm 0.2$ cm

$D = 2 \pm 0.01$ mm

$E_s = 1.72 \pm 0.03$ GPa

147   **Fig. 2** Photos showing (a) the live plant and (b) model plant in the individual plant experiment

148   (IE). The plant properties are shown in the corresponding Figure. ρ is the plant material density,

149   the subscript l and s denote parameters for the leaves and stem, respectively. E is the elastic

150   modulus, l is the element length, b and d are the width and thickness of the leaf. D is the stem

151   diameter.

152

153   IE tested 4 water depths, $h = 27$, 36, 40, and 45 cm for the live and full model plant. The leaf

154   and stem only tests were down under $h = 45$ cm. Note that the leaf data reported here corresponds

155   with an initial vertical leaf posture, and the leaf width was oriented perpendicular to the wave

156   propagation direction (i.e., leaf posture 1 in Figure 4a in Zhang and Nepf, 2021). Three wave

157   periods, $T_w =$2.01, 1.44, and 1.12 s, and six wave amplitudes were tested. The tests include the

158   pure wave experiment reported in Zhang and Nepf (2021) and the combined current and wave

159   experiments reported in Zhang and Nepf (2022). In addition, there are 28 unreported cases (6

160   model plant cases and 22 live plant tests). The case names were formed by the type of plant (Live,

161   Leaf, Stem, Model), the water depth (h27, h36, h40, h45), the wave frequency (f05, f07, and f09),

162   and the wave height level (W1, W2, W3, W4, W5, W6, W7). The current conditions were labeled

163   by pump frequency (10 to 50 Hz), C1, C2, C3, C4, and C5. For example, Leaf_h45_f05_C1W1

164   corresponds to the test for an individual model leaf under water depth $h = 45$ cm, $T_w =$2.01 s

165   (wave frequency is 0.5 Hz), current pump frequency set to 10 Hz and the smallest wave height

166   (wave amplitude $a_w \approx 1$ cm). Considering all the IE tests, the wave orbital velocity $U_w = 4$ to 24

167   cm/s, and the channel-average current $U_c = 3$ to 18 cm/s. The current to wave velocity ratio

168   spanned $U_c/U_w = 0.16$ to 4.7, covering a range of conditions present in the field (Garzon et al.,

169   2019b).

170   The force sensor and wave gauge were controlled by a Labview program which enabled high

171   quality synchronous measurement. Both the drag force and wave height were measured at a

172   sampling rate of 2000 Hz and for a duration of 3 minutes. During the force and wave gauge

173   measurements, a smart cellphone (MIX 2S) camera was used to record a 10-second UHD 4k video

174   at 30 fps, which covered 5 to 10 wave periods, depending on the wave period. The camera was

175   fixed to a tripod through a self-stick holder such that the videos for each plant have the same

176   window. The videos for all tests are available at: https://doi.org/10.6084/m9.figshare.24117324.

177   After the force measurements, the plant and force sensor were removed, and a Nortek Vectrino+

178   was used to measure the velocity profile 10 cm upstream of the position where the plant had been

179   to avoid the hole through which the plant was attached. The vertical resolution of the velocity

180   profile was 1 cm. At each measurement point, the Vectrino recorded a 3-min record at 200 Hz.

181

2.2 Meadow experiment setup

In the meadow experiment (ME), the same model plants used in IE (Fig. 2b) were arranged in a staggered array with a meadow density of 280 plants/m^2 (Fig. 3). Once inserted, the erect plants were 30-cm tall. The plants were distributed across the channel width and over a streamwise distance of 3.8 m.
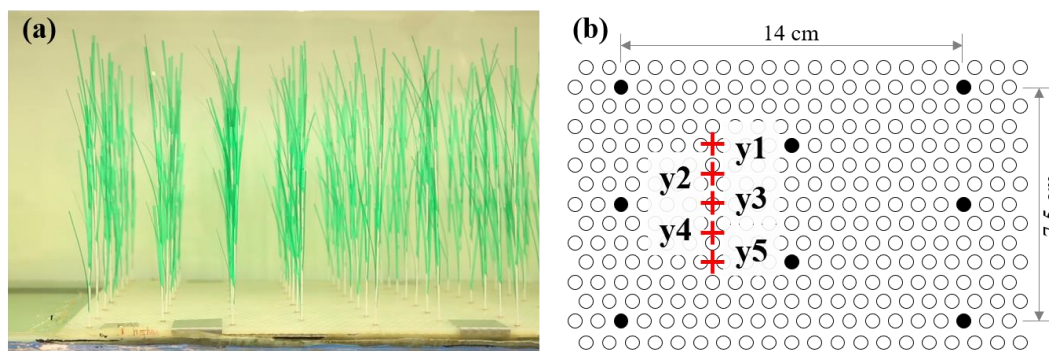
Fig. 3 a) Photo of the model plants, b) section of the baseboard with staggered holes (circles) and the plant positions within the hole array (filled circles)

ME tested five water depths, $h = 18, 27, 36, 40,$ and 45 cm, three wave periods, $T_w = 2, 1.4,$ and 1.1 s, five wave amplitude levels, and three current magnitudes. Similar to the IE cases, the case names were formed based on the flow conditions, e.g., h45_f07_C1W2. In each case, two wave gages were synchronized to measure the free surface displacement at a reference position (wave gauge 1 at $x = -4$ m) and at positions along a transect through the canopy (wave gauge 2). During each experimental run (about 90 min), the wave amplitude at wave gage 1 varied by less than 3%, confirming stationary wave conditions. Wave gage 2 collected data at $x = -4$ to 4 m at 10 and 15 cm intervals. The leading edge of the meadow was located at $x = 0$, such that $x < 0$ was over bare bed. At each position, the free surface displacement, $\eta(t)$, was recorded at 2000 Hz for 1 minute. Additional measurements of wave amplitude were made without plants to assess the wave decay associated with the channel wall and baseboards alone.

Two Nortek Vectrino+ were used to measure the velocity profiles with 1 to 2 cm vertical resolution at P1 (upstream of the meadow) and P2 (within the meadow) (Fig. 1b). At each measurement point, the Vectrino+ recorded a 1-min record with a sampling frequency of 200 Hz. Upstream of the meadow velocity was measured at the channel centerline. Inside the meadow,

206 velocity measurements were made at one (y2 or y4 in Fig. 3b, as in Zhang et al., 2022, 2021) or

207 five lateral locations near the flume centerline (red pluses in Fig. 3b, as in Zhang and Nepf, 2021a).

208

209 2.3 Data analysis

210 The free surface displacement, force, and velocity data were processed in a similar fashion.

211 First, the analysis of wave data will be described in detail. The wave gauge has an accuracy of 0.2

212 (0.7) mm on average (maximum) based on the standard deviation of the raw data under still water

213 conditions. For each record, the mean surface position was removed from the time series to obtain

214 the free surface displacement data η. The surface displacement time series was separated into

215 phase bins following (Lei and Nepf, 2019b; Zhang and Nepf, 2021a). Specifically, for sampling

216 duration T, a wave measurement record contains $M = \text{floor}(T/T_w)$ wave periods, with floor()

217 denoting a downward rounding function. Each wave period contains $\gamma = T_w f_s$ samples and thus γ

218 phase bins. f_s is the sampling frequency. The phase-averaged free surface displacement in the nth

219 phase bin ($n = 1$ to floor(γ)), corresponding to phase $\phi = 2\pi n/\gamma$, was defined as,

$$\breve{\eta}(\phi(n)) = \frac{1}{M}\sum_{m=0}^{M-1}\eta(n+\gamma m) \tag{1}$$

221 $\breve{}$ denotes the phase-averaged value. Within each phase bin, the standard deviation of $\breve{\eta}$ was 0.7

222 (3.6) mm on average (maximum) based on the IE tests. Increasing current intensity led to higher

223 uncertainty in $\breve{\eta}$. The wave amplitude a_w was calculated from the root-mean-square surface

224 displacement,

$$a_w = \sqrt{\frac{2}{\gamma}\sum_{n=1}^{\gamma}\breve{\eta}(\phi(n))^2} \tag{2}$$

226 For ME, the spatial evolution of wave amplitude can be used to estimate the wave damping

227 by vegetation. However, note that the wave amplitude reflected the sum of the incoming wave and

228 the beach-reflected wave, the superposition of which results in an amplitude modulation at an

229 interval of $\lambda/2$ (with wavelength λ, e.g., Fig. 4). Accounting for the wave modulation, the wave

230 decay coefficient K_{Df} was estimated by fitting the measured amplitudes (Lei and Nepf, 2019b),

$$\frac{1}{a_{w,x}} = K_{Df}x + C_1\cos(2kx + \epsilon) + C_2 \tag{3}$$

232 in which $k = 2\pi/\lambda$ is the wavenumber, and ϵ, C_1, and C_2 are fitting parameters. Examples are

233 shown in Fig. 4. Wave decay attributed to the plants (K_D [m^{-2}]) was obtained by subtracting the

234 decay coefficient obtained in the flume without plants.
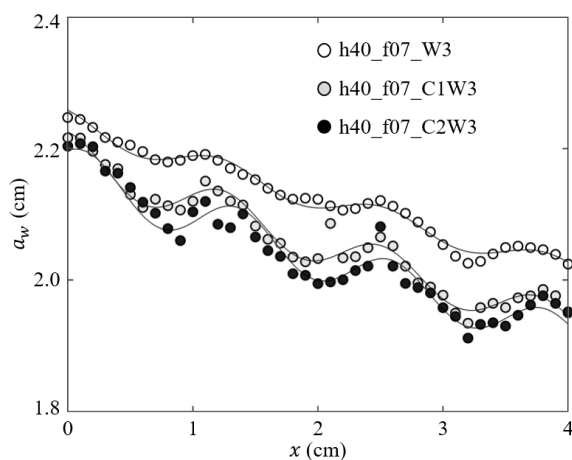
Fig. 4. Measured wave amplitude (symbols) and the fitted Eq. 3 (curves) for h40_f07_W3, h40_f07_C1W3, and h40_f07_C2W3 with the similar wave amplitude but increasing current. (adapted from Figure 4 in Zhang and Nepf, 2021a)

For the individual plant experiments, a time lag of $dt = 74 \pm 4$ ms was determined between the force sensor and wave gauge on average (SD) due to the difference in the instruments' reaction time. This time lag was accounted by removing the free surface displacement records (about 148 data points) before the first force sensor record. The FFT (fast Fourier transform) function in MATLAB was used to filter out high-frequency noise (frequency components greater than 2 Hz), which was negligible based on the frequency spectrum and was subtracted from the raw data. The plant force time series, F, was obtained by removing the offset measured with still water conditions. The phase-averaged plant drag, $\breve{F}$, was obtained in similar way as Eq. 1. The maximum, minimum, and mean value of $\breve{F}$ are reported as F_{max}, F_{min}, and F_m, respectively. For pure current conditions, F_m, was defined by the average over the 3-minute record.

Based on the standard deviation among ten still water measurements, considering different water depth and different plants installed on the force sensor, the accuracy of the force measurements was determined to be 0.001 N (0.002 N) average (maximum). The force exerted on the post alone (without plant) was less than 3% of the force on the model plant (Zhang and Nepf, 2021b, 2022). Consequently, in this dataset, the force due to the post was neglected and not subtracted from the measurements. However, note that the force on the post can contribute up to

256 30% of the total force measured for an individual leaf. Hence, when using the leaf force data, it
257 may be necessary to exclude the force due to the post.

258 For all velocity data, two despiking methods were applied to identify abnormal data points,
259 which were replaced by a NAN (not a number) value. Firstly, data points were identified if the
260 associated acceleration exceed the gravitational acceleration. Second, a threshold, $\pm 3\sigma$ with σ the
261 standard deviation, was applied to identify abnormal data within each phase bins for conditions
262 with waves and in the whole time series for the pure current cases (Zhang and Nepf, 2022). The
263 despiked velocity data is denoted u, v, w, respectively, for the longitudinal, lateral, and vertical
264 directions. For the horizontal velocity component, the velocity data was separated into a phase
265 averaged value $\breve{u}(\phi)$ and a turbulent velocity fluctuation u',

266
$$u = \breve{u}(\phi) + u' = u_m + \breve{u}_w(\phi) + u' \tag{4}$$

267 $\breve{u}(\phi)$ was calculated in the same manner as Eq. 1, and then further separated into a time mean
268 velocity $u_m = \frac{1}{2\pi}\int_0^{2\pi}\breve{u}(\phi)d\phi$ and a wave orbital velocity $\breve{u}_w(\phi) = \breve{u}(\phi) - u_m$. The magnitude of
269 wave orbital velocity was defined as

270
$$u_w = \sqrt{2\frac{1}{2\pi}\int_0^{2\pi}(\breve{u}_w(\phi))^2 d\phi} \tag{5}$$

271 The root mean square of fluctuations within each phase bin (e.g., $u_{rms} = \sqrt{\frac{1}{n}\sum_1^n u'^2}$) was used
272 to estimate the turbulent kinetic energy in that phase bin, $tke(\phi) = (u_{rms}^2 + v_{rms}^2 + w_{rms}^2)/2$.
273 The time-average turbulent kinetic energy, TKE, was defined as the average of $tke(\phi)$ over all
274 phases. The depth- and phase-averaged horizontal velocity was defined as $\breve{U} = \frac{1}{h}\int_0^h\breve{u}(\phi,z)dz$.
275 The depth-average velocity statistics reported for each velocity profile includes the maximum
276 U_{max}, minimum U_{min}, and mean U_m value of $\breve{U}$. The depth-average wave orbital velocity was
277 defined as $U_w = \sqrt{2\frac{1}{2\pi}\int_0^{2\pi}(\breve{U} - U_m)^2 d\phi}$. For the pure current cases, $U_m = U_c$ was defined by
278 the depth- and time-averaged velocity over the whole measurements. Note that the phase-averaged
279 and depth-averaged values for the lateral (v) and vertical (w) velocity components were calculated
280 in the same way as the horizontal component.

281

3. Data

3.1 Data for the individual plant experiments (IE)

In experiments with individual plants, the plant force and free surface displacement at the same streamwise (x) location as the plant were measured simultaneously. The motion of plant was captured in videos during the force measurement. The flow velocity was measured separately, but assumed to be in-phase with the free surface displacement. These data contained all relevant parameters necessary for understanding the hydrodynamic performance of an individual marsh plant. For example, Fig. 5 shows the maximum plant motion, phase-averaged plant drag and free surface displacement, as well as the phase- and depth-averaged velocity for the model plant under the same wave with and without following current. These data demonstrate a strong dependence of plant force on the instantaneous flow velocity, which can be utilized to validate predictions of plant drag, as in Zhang and Nepf (2022, 2021b). It is worth noting that the phase-averaged data allows for detailed validation of phase resolving models. Few studies, e.g., Jacobsen et al. (2019); Luhar and Nepf (2016), have reported time-varying velocity and force on flexible plants. However, for modeling and validating of plant motion and time-varying plant force, high-resolution time-varying horizontal and vertical velocity are required. For example, Zhu et al. (2020) demonstrated that the vertical velocity results in asymmetric plant motion, even when subjected to symmetric waves. For high resolution model validation, the present dataset includes both the time-varying horizontal and vertical velocity, as well as the synchronized force and free surface displacement for both live and model plants.
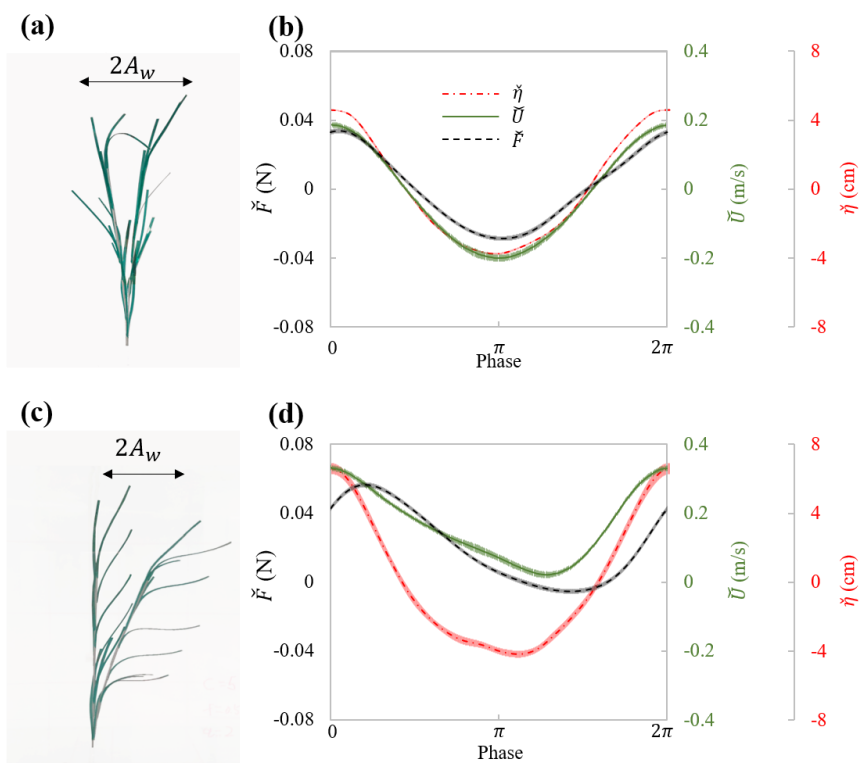
Fig. 5 Plant motion and phase-averaged measurements of force (black curve), surface displacement (red curve) and velocity (green curve) for (a) and (b) model_h45_f05_W5 (U_m = -1.9 cm/s, and U_w = 19.1 cm/s); and (c) and (d) model_h45_f05_C5W5 (U_m = -16.3 cm/s, and U_w = 14.3 cm/s). (a) and (c) showed the digital image of model plant at the maximum downstream and upstream posture within the wave cycle. The thin shading in each curve in subplots (b) and (d) indicate the uncertainty in each phase. (modified based on figure 5 in Zhang and Nepf, 2022).

The force measurements suggested that sheltering and interaction among the leaves and stem decreased the force exerted on the full plant compared to the leaves and stem in isolation (Fig. 6a). The decrease in plant drag can be represented by a constant sheltering coefficient C_s for a given plant morphology. Specifically, for a plant with N_l leaves attached to a central stem, the force of on the full plant is: F(plant) = C_s × F(one leaf)× N_l + F(stem), with C_s =0.6 for the model plant reported here (Zhang and Nepf, 2021b). The leaves was estimated to contributed 72% ± 1% of the plant-scale drag (Zhang and Nepf, 2021b). With this finding, the hydrodynamic force on a plant

317   with complex leaf and stem morphology can be easily estimated using the force prediction for an

318   individual simple structure (a flat leaf or a cylindrical stem, e.g., the models described in Zhu et

319   al., 2020; Mullarney and Henderson, 2010; Luhar and Nepf, 2011, 2016)).

320   The maximum force on the plant is plotted against the maximum depth- and phase-averaged

321   velocity in Fig. 6. Note that for $h = 40$ and 45 cm, both the live and model plant were submerged

322   at the wave crest (see videos in https://doi.org/10.6084/m9.figshare.24117324). The maximum

323   force for these two water depth follow the same trend with velocity (Fig. 6b and c). For smaller

324   water depth, only part of the plant was submerged, such that the plant felt smaller force under

325   similar horizontal velocity (Fig. 6b and c). The relationship between F_{max} and U_{max} is similar for

326   different current velocity, but curves are shifted to the right as current increases (darker symbols

327   in Fig. 6d), i.e., as current magnitude increases a greater U_{max} is needed to reach the same F_{max}

328   (Fig. 6 d).
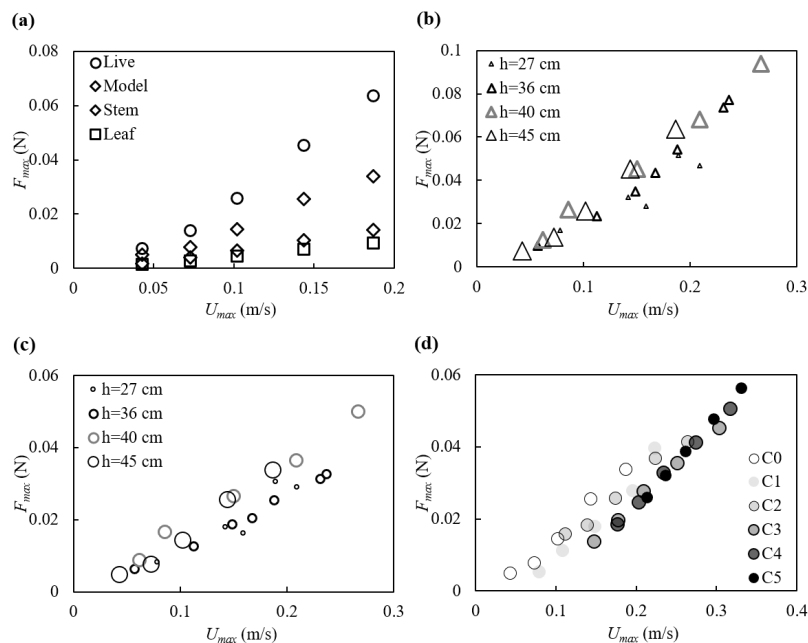
329

330   **Fig. 6** maximum force on the plant plotted against the maximum horizontal velocity for (a) all

331   plants at $h = 45$ cm, (b) the live plant and (c) the model plant under pure waves, (d) the model plant

332   at $h = 45$ cm under combined current and waves with increasing current intensity labeled by C0 to

333   C5. All the cases shown are associated with wave frequency $f = 0.5$ Hz.

334

3.2 Canopy velocity structure and turbulence

The canopy velocity structure and turbulence were altered by the plant drag, which in turn affects the dissipation of wave energy. Fig. 7 shows a few examples of the turbulence and velocity structure of the ME test. First, for pure current, the presence of the canopy significantly modified both the flow structure and turbulent intensity (Fig. 7a). The time-mean velocity u_m at P1 (2 m upstream of the meadow) exhibited a boundary-layer velocity profile (circles in Fig. 7a2), and the TKE was essentially uniform, with a slight increase near the bed (circles in Fig. 7a1). The canopy resistance reduced u_m within the canopy height by a factor of 0.29 and redirected the time-mean flow above the canopy, forming a shear layer extending from the top of the stems toward the free surface (Fig. 7a2). Within the stem height, the magnitude of the horizontal velocity was negatively correlated to the distribution of plant frontal area (Nepf, 2012). Specifically, a greater time-mean velocity was observed near the bed (Fig. 7a2) where the plant frontal area was smaller (Fig. 2b). Considering that the velocity is zero at the bed, the velocity profile u_m exhibited an "S" shape at P2 (2.46 m inside the meadow). The time-mean velocity u_m at five lateral locations within the canopy (y1 to y5, red pluses in Fig. 3b) were the same within uncertainty, but the TKE was maximum directly upstream of a plant (P2_y1 and P2_y5) and minimum directly downstream of a plant (P2_y3). The maximum TKE was observed near the top of the canopy due to shear production associated with the strong vertical gradient in velocity (Fig. 7a2).

For pure waves, the turbulence intensity was maximum near the free surface and decreased with distance from the surface at P1 (circles in Fig. 7b1). Note that the time-mean velocity can be slightly negative in a closed flume, reflecting the return current that develops to balance the mass transport associated with the Stokes draft (Monismith, 2020), and its magnitude increases with distance from the bottom (Fig. 7b2). The presence of the canopy reduced the wave orbital velocity u_w slightly due to the wave energy dissipation by the plants (Fig. 7b3) and adjusted the time-mean velocity to a more uniform profile (Fig. 7b2). Compared to TKE measured at P1, the turbulent intensity at P2 was larger within the canopy, but similar near the top of the canopy (Fig. 7b1). Specifically, above the canopy height, TKE was primarily generated by the shear gradient, and the similar TKE at P1 and P2 can be explanted by the comparable time-mean velocity profiles. Within the canopy, TKE was mainly generated by the plant form drag, such that TKE was obviously larger compared to P1.
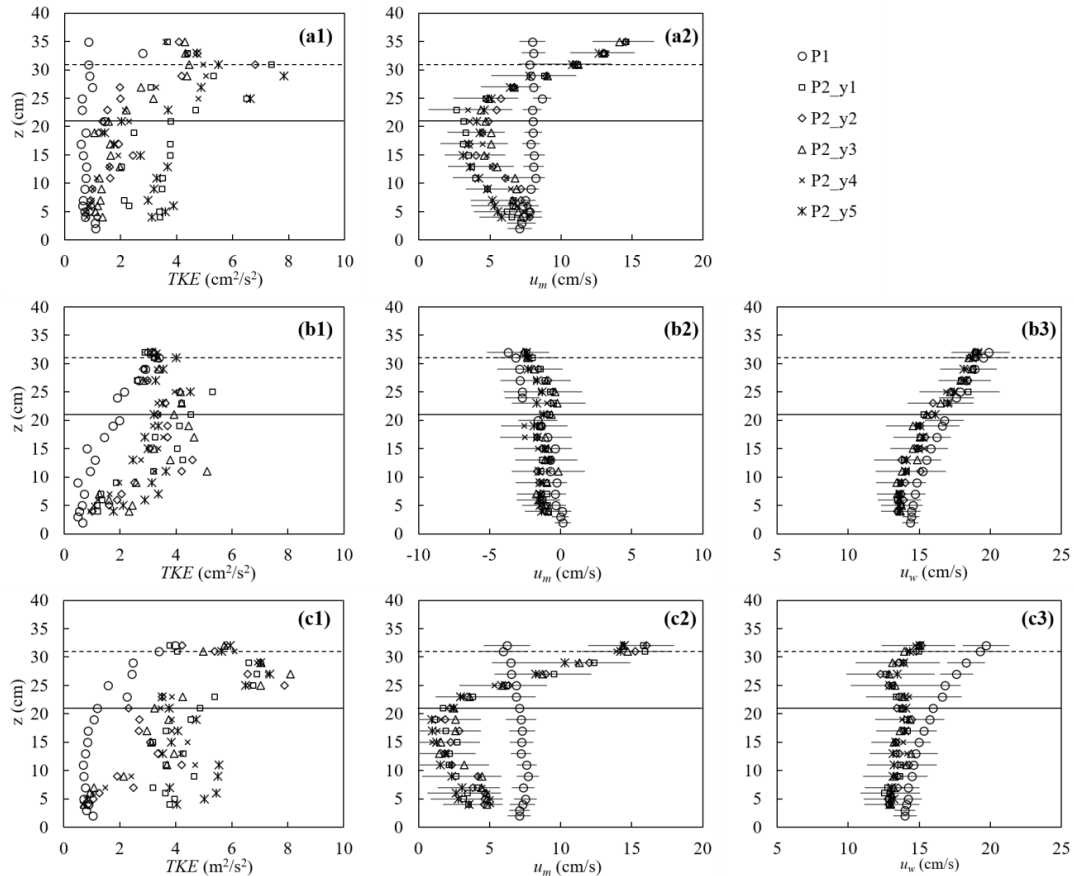
Fig. 7 The turbulent kinetic energy (left), horizontal time-mean velocity (middle), and wave orbital velocity (right column) for (a) pure current (h40_C2, U_m = 7.7 cm/s), (b) pure waves (h40_f07_W5, U_m = -1.8 cm/s, U_w = 16.7 cm/s), and (c) combined current and waves (h40_f07_C2W5, U_m = 7.0 cm/s, U_w = 15.6 cm/s). For the cases shown, water depth h = 40 cm. The measurements were made at P1 (2 m in front of the meadow at flume central) and P2 (2.46 m in the meadow) at five lateral positions y1 to y5 shown as red plus signs in Fig. 3b. The horizontal bars indicate the average standard deviation within each phase bins. The solid and dashed horizontal lines indicate the stem height and erect canopy height, respectively.

Finally, consider the conditions with combined current and waves (Fig. 7c). Upstream of the canopy (position P1, open circles in Fig. 7), the time-mean velocity u_m (Fig. 7c2) and wave velocity u_w (Fig. 7c3) exhibited the same vertical profile shape as that observed for the pure

379   current (Fig. 7a2) and pure wave conditions (Fig. 7b3), respectively, and TKE (Fig. 7c1) was

380   similar in magnitude to the pure wave condition (Fig. 7b1). This might be explained by time-mean

381   velocity gradients (Fig. 7c2 and 7b2), which feed shear-production of turbulence, are similar in

382   pure wave and combined wave-current conditions. Within the meadow (P2), adding current

383   resulted in greater decrease in u_w and with more uniform profile (Fig. 7c3), compared to that under

384   pure waves (Fig. 7b3). Smaller in-canopy wave orbital velocity was explained by greater plant

385   drag (positively related to $u_m + u_w$ as in Fig. 6) and hence greater wave energy dissipation under

386   combined conditions than the same pure wave (Zhang and Nepf, 2021a). Similarly, stronger plant

387   resistance under combined current and waves resulted in a greater reduction in time-mean velocity

388   within the canopy, relative to upstream, compared to pure current conditions (Fig. 7c2).

389   Specifically, for the combined wave-current conditions, u_m within the canopy (roughly $z <30$ cm)

390   at P2 was reduced by a factor of 0.42, compared to u_m at P1. Whereas for the pure current

391   condition the reduction was only a factor of 0.29. Finally, in combined wave-current conditions,

392   the TKE within the meadow (P2) was greater than TKE for either the pure current or pure wave

393   conditions (comparing the left column in Fig. 7). This was consistent with the greater reduction in

394   in-canopy current and greater dissipation of wave energy, because energy lost from time-mean and

395   wave energy is converted in turbulent kinetic energy. In addition, in the combined wave-current

396   conditions two regions of high TKE were observed, one near the top of the canopy, associated

397   with shear-generated turbulence and consisted with the pure current condition, and a second within

398   the lower canopy, associated with plant element-generated turbulence (Fig. 7c1).

399   In addition to the time-mean velocity, wave-orbital velocity, and turbulent kinetic energy, the

400   time series for each velocity component (u, v, w) as both raw data and phase-averaged velocity for

401   all ME are contained in the dataset. This dataset can be used to disclose more physical mechanisms

402   behind current-wave-vegetation interaction.

403

3.3 Wave decay over salt marsh meadow

405   ME measured the free surface displacement at 2000 Hz, with a spatial interval of 10 or 15 cm

406   along the meadow length. These data can be used to examine the wave amplitude dissipation (as

407   in Zhang et al., 2021, 2022; Zhang and Nepf, 2021a) and wave shape transformation over a salt

408   marsh meadow. The wave decay coefficient, K_D, increased with decreasing water depth and

409   decreasing wave amplitude (Fig. 8). For a constant water depth (circles in Fig. 8), as wave period

410   increased from T_w =1.12 s to 1.44, K_D increased, but then remained the same within uncertainty

411   between T_w = 1.44 and 2.01 s. The dependence of K_D on water depth, wave amplitude, and wave

412   period can be explained by how these parameters affect the fluid velocity and drag on the plant.

413   First, for the same a_w and T_w, U_w increases with decreasing h, generating greater plant drag and

414   thus greater wave energy dissipation as water depth decreases. Second, for a constant depth ($h =$

415   45 cm) and wave amplitude, an increase in wave period (here, T_w =1.11, 1.44, and 2.01 s) produces

416   a decrease in dimensionless wave number kh = 1.55, 1.08, and 0.77, respectively. This decrease in

417   kh is associated with wave velocity profile that is increasingly more uniform, producing larger

418   depth-averaged velocity magnitude (see Figure B.1 in Zhang et al., 2022). Finally, with constant

419   depth and wave period, an increase in wave amplitude results in greater plant motion within the

420   wave cycle, which increased the plant drag reduction (due to greater plant reconfiguration) and

421   wave dissipation. Detailed mechanisms and scaling analysis was provided in Zhang et al. (2022).
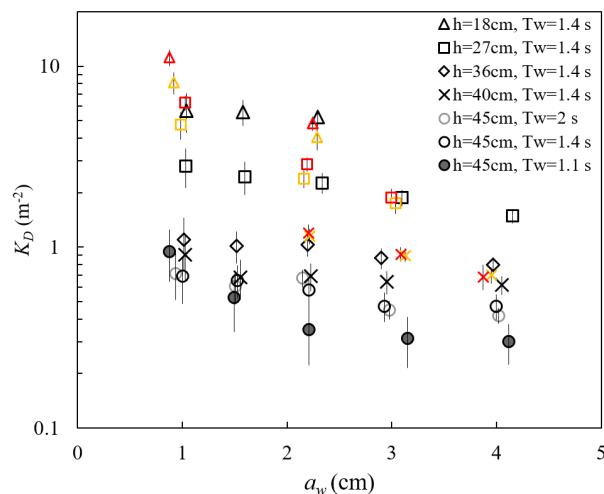

422

423   **Fig. 8** Wave decay coefficients K_D for all cases reported in the (Zhang and Nepf, 2021a; Zhang et

424   al., 2021, 2022). The yellow and red symbols indicated waves with small (U_c = 4.7 cm/s) and

425   larger (U_c = 7.8 cm/s) following current, respectively. The vertical bars indicate uncertainty in K_D.

426   (adopted from Figure 4a in Zhang et al., 2021)

427

428   Adding a following current tended to increase wave dissipation. For the same water depth and

429   wave period, K_D increased with increasing current magnitude (red and yellow symbols in Fig. 8),

430   compared to pure wave conditions (black symbols in Fig. 8) with similar wave amplitude. The

431   effect of a following current increasing wave dissipation is shown more clearly in Fig. 9. There

432   were a few exceptions for $U_c/U_w < 0.6$, for which adding current slightly reduced the wave decay

433   coefficient, i.e., $K_{D,cw}/K_{D,pw} < 1$. Opposite effect of current on wave decay has been reported in a

434   few studies (Hu et al., 2014; Li and Yan, 2007; Yin et al., 2020; Paul et al., 2012; Losada et al.,

435   2016; Zhao et al., 2020). Paul et al. (2012) attributed the reduction in wave dissipation with current

436   mainly to an observed reduction in plant motion. However, for rigid canopies, following current

437   was also observed to reduce wave dissipation when U_c/U_w smaller than a transition value of 0.65

438   to 1.25 (Hu et al., 2014) and 0.37 to 1.54 (Yin et al., 2020), but increased above pure wave

439   ($K_{D,cw}/K_{D,pw} > 1$) for higher following currents (Hu et al., 2014; Li and Yan, 2007; Yin et al.,

440   2020). With an opposing current, wave dissipation was enhanced and to a higher degree compared

441   to that of the following current of similar magnitude (Hu et al., 2021).
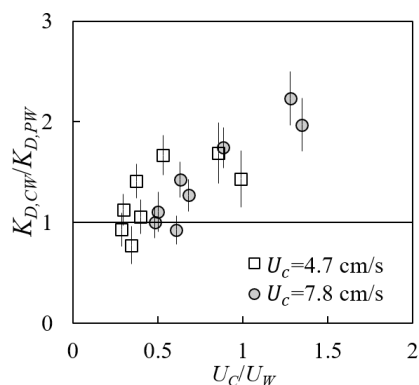
442

443   **Fig. 9** Ratio of wave decay coefficients under combined condition to pure wave condition plotted

444   against the ratio of current to wave velocity. (adopted from Figure 6a in Zhang and Nepf, 2021a)

445

446   Based on our laboratory measurements and theoretical analysis, we explained the different

447   observed effects of current on wave dissipation as the result of the following competing

448   mechanisms. First, consider that the wave energy was only dissipated by plants, the time rate of

449   energy dissipation scales with plant drag and canopy total velocity $E_D \sim F_D U$. Adding current

450   increases the total fluid velocity (Fig. 7) and thus the total plant force (Fig. 6), resulting in a greater

451   wave energy dissipation, compared to the same pure wave. Second, the influence of current on

452   wave dissipation is further modulated by the effect of plant resistance on the time-mean canopy

453   flow structure (Fig. 7). In particular, the time-mean velocity within the canopy is significantly

454 reduced compared to velocity upstream of the canopy at the same distance from the bed (P1 in Fig.

455 7). A reduction in time-mean velocity in the canopy, relative to the depth-averaged, time-mean

456 velocity, decreases the impact of current on wave decay. Because the in-canopy current has a

457 greater reduction for a denser canopy, the influence of current on wave decay is diminished for a

458 denser canopy, relative to a more sparse canopy. Third, a current changes the celerity of wave

459 energy propagation, i.e., the wave group velocity $C_g = C_{g,pw} + U_c$, which connects the time-rate

460 of wave energy dissipation to the spatial rate of wave energy dissipation (represented by K_D). For

461 the same $|U_c|$ and plant drag (associated with the same E_D), an opposing (following) current

462 decreases (increases) C_g and generates larger (smaller) K_D (spatial rate of amplitude decay).

463 For the experiments describe here, conducted in a finite length channel, the time-mean

464 velocity is slightly negative for pure waves (Fig. 7b2), such that adding small following current

465 could lead to a decrease in the magnitude of time-mean velocity. Further increase in the current

466 magnitude would increase the magnitude of time-mean and total velocity, which is why the present

467 and previous studies (Hu et al., 2014; Yin et al., 2020) observed a reduction in K_D only under small

468 following current, with a larger following current increasing K_D, compared to the same pure wave.

469 The greater increase in K_D under opposing current than following current with the same magnitude,

470 as observed in (Hu et al., 2014; Yin et al., 2020), can be explained by the effect of current direction

471 on wave group velocity (the third mechanism above). The decrease in K_D observed in highly

472 flexible seagrass mimics (Paul et al., 2012) under following current might be explained by the

473 weaker increase in plant drag and canopy flow velocity (associated with limited increase in the

474 time-rate energy dissipation), and the decrease in K_D due to an increase in wave group velocity C_g

475 (the third mechanism above), compared to pure wave conditions. Specifically, increasing current

476 led to a more pronated plant posture and enhanced force reduction in flexible leaves, compared to

477 the leaf under the same pure wave (see Figure 6 and table 1 in Lei and Nepf, 2019a). Further, the

478 time-mean velocity within the canopy height is smaller under combined current and waves than

479 current along with the same magnitude (see Fig. 7a2 and 7c2), and the canopy time-mean velocity

480 reduction is further enhanced by the decrease in canopy height due to plant reconfiguration (greater

481 plant solid volume fraction within the canopy height).

482

4. Data availability

All instrument measured data presented in this paper are available from Figshare (https://doi.org/10.6084/m9.figshare.24117144; Zhang and Nepf, 2023a). The repository includes the raw time series, phase-averaged, and various statistical metrics (time-mean, maximum, minimum) of force, surface displacement, and velocity. A data instruction in the readme file is also included in the repository. The plant motion recorded in the individual plant experiments can be found at: https://doi.org/10.6084/m9.figshare.24117324; Zhang and Nepf, 2023b.

5. Recommendations for data reuse

5.1 Plant dynamic model validation

The plant motion videos, phase-resolving plant drag, free surface displacement, and 3D velocity data can be used to validate phase-resolving plant dynamic models. The time-averaged force and velocity statistics can be used to validate phase-averaged plant drag models (as in Zhang and Nepf, 2021b, 2022). This dataset includes a new data not included in Zhang and Nepf (2021 and 2022) associated with strongly nonlinear waves, which can be applied to reveal the nonlinear effects on plant motion and drag.

The measurements also captured a phase lag between the plant force and wave motion (reflected by the free surface displacement). The presence of a following current tended to increase the magnitude of this phase lag (Fig. 5). The dataset in Hu et al. (2021) also contained time lags between the wave (velocity) and force data (Figure 5 in their paper). However, their wave and force data were not measured simultaneously so the source of phase lag was unclear. Using a high-resolution synchronization method, Jacobsen et al. (2019) were able to capture the phase lag between the motion of an individual flexible leaf and the fluid velocity, which disclosed an important knowledge gap in describing the physical cause of the observed phase lag. The present dataset can be used to deepen our understanding in the plant motion and force in response to waves with and without current in high temporal resolution.

5.2 Flow structure within salt marsh meadow

The drag associated with a canopy has long been known to modify the vertical structure of current and wave velocity (Chen et al., 2013; Lowe et al., 2005; Zeller et al., 2015; Lei and Nepf, 2021), but few data have been reported under combined current and waves. The present dataset

514   reveals the flow structure within marsh canopies under pure current, pure wave, and their
515   combination. Lowe et al. (2005) showed that a submerged canopy is more efficient in reducing the
516   time-mean velocity than the wave orbital velocity. They developed a 2-layer model to predict the
517   canopy wave orbital velocity without considering the influence of current. Zeller et al. (2015)
518   developed a prediction for the canopy total velocity under combined current and waves. However,
519   their model was only validated using five flow conditions in a rigid canopy. Further, previous
520   studies of canopy velocity structure seldom compare the reduction of time-mean and wave orbital
521   velocity using laboratory data measured under current and waves acting alone and in combination.
522   The present dataset ME measured high resolution velocity profiles upstream (single profile) and
523   within (five lateral locations) a meadow under combined current and wave conditions (e.g., Fig.
524   7). The dataset covers water depth to plant height ratios from emergent to submerged and velocity
525   ratios $U_c/U_w = 0.16$ to 4.7. Measurements were also made using the same current and wave acting
526   alone. This dataset can be utilized to study the interaction between current and waves, e.g., the
527   canopy time-mean velocity was found to be reduced when waves are present (Fig. 7b2 and c2).
528   The dataset can also be used to validate theoretical and numerical models that predict canopy
529   current and wave velocity.

5.3 Turbulent kinetic energy due to salt marsh

531   As shown in Fig.7 and described in section 3.2, the presence of marsh plants significantly
532   enhanced turbulence intensity. For current over bare beds, turbulence is generated by spatial
533   gradients in time-mean velocity (shear production) and the TKE is essentially uniform, except very
534   close to the bed (circles in Fig. 7a1). However, when waves are presented, TKE was maximum
535   near free surface and decreased away from the surface (circles in Fig. 7b1 and c1), possibly due to
536   time-mean shear introduced by the return current associated with wave conditions (circles in Fig.
537   7b3 and c3). Within the meadow, the TKE varied with position relative to individual plants. TKE
538   was largest under combined current and wave conditions (compare the left column in Fig. 7), with
539   turbulence peaks observed near the top of the canopy, associated with shear-production by the
540   time-mean current, and within the canopy, associated with turbulence production in the wakes of
541   individual plants (Fig. 7c1). This dataset can be used to develop and validate models to predict
542   canopy turbulence (e.g., Xu and Nepf, 2020) and for use in numerical models (e.g., Tang and Lin,
543   2021).

5.4 Wave decay over salt marsh meadow

The meadow experiments (ME) measured the free surface displacement along the length of the meadow with a horizontal interval of 10 and 15 cm, which included 18 to 26 points within one wave length (see Figure C.1 in Zhang et al., 2022). The raw time-series data can be utilized to analyze the transformation of wave shape, including wave skewness and wave asymmetry, over salt marshes. The wave shape is a crucial parameter when describing wave-driven sediment motion and hence important for the study of coast stability within salt marsh regions.

The wave dissipation dataset presented here adds to the dataset reported in Hu et al. (2021), expanding the range of conditions. Specifically, Hu et al. (2021) reported wave decay data over rigid cylinders, while the present dataset provides wave decay over model plants with more realistic morphology. The dataset can be applied to validate phase-averaged (e.g., Garzon et al., 2019a; Smith et al., 2016) and phase-resolving coast models (e.g., Chen and Zou, 2019; Mattis et al., 2019) in predicting the wave energy reduction by salt marshes.

Author contributions. ZXX designed the experiments, conducted the experiments and collected the raw data. ZXX prepared the manuscript, NH review and edit the manuscript.

Competing interests. The contact author has declared that neither they nor their coauthors have any competing interests.

6. References

Barbier, E. B., Hacker, S. D., Kennedy, C., Koch, E. W., Stier, A. C., and Silliman, B. R.: The value of estuarine and coastal ecosystem services, Ecological Monographs, 81, 169–193, https://doi.org/10.1890/10-1510.1, 2011.

Boesch, D. F. and Turner, R. E.: Dependence of fishery species on salt marshes: The role of food and refuge, Estuaries, 7, 460–468, https://doi.org/10.2307/1351627, 1984.

Chen, H. and Zou, Q.: Eulerian–Lagrangian flow-vegetation interaction model using immersed boundary method and OpenFOAM, Advances in Water Resources, 126, 176–192, https://doi.org/10.1016/j.advwatres.2019.02.006, 2019.

577   Chen, Z., Jiang, C., and Nepf, H.: Flow adjustment at the leading edge of a submerged aquatic canopy,
578   Water Resour. Res., 49, 5537–5551, https://doi.org/10.1002/wrcr.20403, 2013.
579   Elschot, K., Bouma, T. J., Temmerman, S., and Bakker, J. P.: Effects of long-term grazing on sediment
580   deposition and salt-marsh accretion rates, Estuarine, Coastal and Shelf Science, 133, 109–115,
581   https://doi.org/10.1016/j.ecss.2013.08.021, 2013.
582   Garzon, J. L., Miesse, T., and Ferreira, C. M.: Field-based numerical model investigation of wave
583   propagation across marshes in the Chesapeake Bay under storm conditions, Coastal Engineering, 146,
584   32–46, https://doi.org/10.1016/j.coastaleng.2018.11.001, 2019a.
585   Garzon, J. L., Maza, M., Ferreira, C. M., Lara, J. L., and Losada, I. J.: Wave attenuation by *Spartina*
586   saltmarshes in the Chesapeake Bay under storm surge conditions, J. Geophys. Res. Oceans, 124, 5220–
587   5243, https://doi.org/10.1029/2018JC014865, 2019b.
588   Gosselin, F., De Langre, E., and Machado-Almeida, B. A.: Drag reduction of flexible plates by
589   reconfiguration, J. Fluid Mech., 650, 319–341, https://doi.org/10.1017/S0022112009993673, 2010.
590   Harder, D. L., Speck, O., Hurd, C. L., and Speck, T.: Reconfiguration as a prerequisite for survival in highly
591   unstable flow-dominated habitats, J Plant Growth Regul, 23, 98–107, https://doi.org/10.1007/s00344-
592   004-0043-1, 2004.
593   Hu, Z., Suzuki, T., Zitman, T., Uittewaal, W., and Stive, M.: Laboratory study on wave dissipation by
594   vegetation in combined current–wave flow, Coastal Engineering, 88, 131–142,
595   https://doi.org/10.1016/j.coastaleng.2014.02.009, 2014.
596   Hu, Z., Lian, S., Wei, H., Li, Y., Stive, M., and Suzuki, T.: Laboratory data on wave propagation through
597   vegetation with following and opposing currents, Earth Syst. Sci. Data, 13, 4987–4999,
598   https://doi.org/10.5194/essd-13-4987-2021, 2021.
599   Huai, W., Li, S., Katul, G. G., Liu, M., and Yang, Z.: Flow dynamics and sediment transport in vegetated
600   rivers: A review, J Hydrodyn, 33, 400–420, https://doi.org/10.1007/s42241-021-0043-7, 2021.
601   Jacobsen, N. G., Bakker, W., Uijttewaal, W. S. J., and Uittenbogaard, R.: Experimental investigation of the
602   wave-induced motion of and force distribution along a flexible stem, J. Fluid Mech., 880, 1036–1069,
603   https://doi.org/10.1017/jfm.2019.739, 2019.
604   Jalonen, J. and Järvelä, J.: Impact of tree scale on drag: Experiments in a towing tank, in: Proceedings of
605   2013 IAHE world Congress, 2013.
606   Keulegan, G. H. and Carpenter, L. H.: Forces on cylinders and plates in an oscillating fluid, J. RES. NATL.
607   BUR. STAN., 60, 423, https://doi.org/10.6028/jres.060.043, 1958.
608   Knutson, P. L., Brochu, R. A., Seeling, W. N., and Margaret, I.: Wave damping in Spartina alterniflora
609   marsh, Wetlands, 2, 87–104, 1982.
610   Lei, J. and Nepf, H.: Blade dynamics in combined waves and current, Journal of Fluids and Structures, 87,
611   137–149, https://doi.org/doi:10.1016/j.jfluidstructs.2019.03.020, 2019a.
612   Lei, J. and Nepf, H.: Wave damping by flexible vegetation: Connecting individual blade dynamics to the
613   meadow scale, Coastal Engineering, 147, 138–148, https://doi.org/10.1016/j.coastaleng.2019.01.008,
614   2019b.
615   Lei, J. and Nepf, H.: Evolution of flow velocity from the leading edge of 2-D and 3-D submerged canopies,
616   J. Fluid Mech., 916, A36, https://doi.org/10.1017/jfm.2021.197, 2021.
617   Li, C. W. and Yan, K.: Numerical investigation of wave–current–vegetation interaction, Journal of
618   Hydraulic Engineering, 133, 794–803, https://doi.org/10.1061/(ASCE)0733-9429(2007)133:7(794),
619   2007.
620   Losada, I. J., Maza, M., and Lara, J. L.: A new formulation for vegetation-induced damping under combined
621   waves and currents, Coastal Engineering, 107, 1–13, https://doi.org/10.1016/j.coastaleng.2015.09.011,
622   2016.
623   Lowe, R. J., Koseff, J. R., and Monismith, S. G.: Oscillatory flow through submerged canopies: 1. Velocity
624   structure, Journal of Geophysical Research: Oceans, 110, https://doi.org/10.1029/2004JC002788,
625   2005.
626   Luhar, M. and Nepf, H. M.: Flow-induced reconfiguration of buoyant and flexible aquatic vegetation,
627   Limnol. Oceanogr., 56, 2003–2017, https://doi.org/10.4319/lo.2011.56.6.2003, 2011.

628   Luhar, M. and Nepf, H. M.: Wave induced dynamics of flexible blades, Journal of Fluids and Structures,
629   61, 20–41, https://doi.org/10.1016/j.jfluidstructs.2015.11.007, 2016.
630   Mattis, S. A., Kees, C. E., Wei, M. V., Dimakopoulos, A., and Dawson, C. N.: Computational model for
631   wave attenuation by flexible vegetation, J. Waterway, Port, Coastal, Ocean Eng., 145, 04018033,
632   https://doi.org/10.1061/(ASCE)WW.1943-5460.0000487, 2019.
633   Maza, M., Lara, J. L., Losada, I. J., Ondiviela, B., Trinogga, J., and Bouma, T. J.: Large-scale 3-D
634   experiments of wave and current interaction with real vegetation. Part 2: Experimental analysis,
635   Coastal Engineering, 106, 73–86, https://doi.org/10.1016/j.coastaleng.2015.09.010, 2015.
636   Monismith, S. G.: Stokes drift: theory and experiments, J. Fluid Mech., 884, F1,
637   https://doi.org/10.1017/jfm.2019.891, 2020.
638   Morison, J. R., Johnson, J. W., and Schaaf, S. A.: The force exerted by surface waves on piles, Journal of
639   Petroleum Technology, 2, 149–154, https://doi.org/10.2118/950149-G, 1950.
640   Mullarney, J. C. and Henderson, S. M.: Wave-forced motion of submerged single-stem vegetation, J.
641   Geophys. Res., 115, C12061, https://doi.org/10.1029/2010JC006448, 2010.
642   Nepf, H. M.: Flow and transport in regions with aquatic vegetation, Annu. Rev. Fluid Mech., 44, 123–142,
643   https://doi.org/10.1146/annurev-fluid-120710-101048, 2012.
644   Paul, M., Bouma, T., and Amos, C.: Wave attenuation by submerged vegetation: combining the effect of
645   organism   traits   and   tidal   current,   Mar.   Ecol.   Prog.   Ser.,   444,   31–41,
646   https://doi.org/10.3354/meps09489, 2012.
647   Pidgeon, E.: Carbon sequestration by coastal marine habitats: Important missing sinks, in: The Management
648   of Natural Coastal Carbon Sinks, 2009.
649   Schoutens, K., Heuner, M., Minden, V., Schulte Ostermann, T., Silinski, A., Belliard, J.-P., and
650   Temmerman, S.: How effective are tidal marshes as nature-based shoreline protection throughout
651   seasons, Limnol. Oceanogr., 64, 1750–1762, https://doi.org/10.1002/lno.11149, 2019.
652   Schoutens, K., Heuner, M., Fuchs, E., Minden, V., Schulte-Ostermann, T., Belliard, J.-P., Bouma, T. J.,
653   and Temmerman, S.: Nature-based shoreline protection by tidal marsh plants depends on trade-offs
654   between avoidance and attenuation of hydrodynamic forces, Estuarine, Coastal and Shelf Science, 236,
655   106645, https://doi.org/10.1016/j.ecss.2020.106645, 2020.
656   Schoutens, K., Luys, P., Heuner, M., Fuchs, E., Minden, V., Schulte Ostermann, T., Bouma, T., Van Belzen,
657   J., and Temmerman, S.: Traits of tidal marsh plants determine survival and growth response to
658   hydrodynamic forcing: implications for nature-based shoreline protection, Mar. Ecol. Prog. Ser., 693,
659   107–124, https://doi.org/10.3354/meps14091, 2022.
660   Schutten, J. and Davy, A. J.: Predicting the hydraulic forces on submerged macrophytes from current
661   velocity, biomass and morphology, Oecologia, 123, 445–452, https://doi.org/10.1007/s004420000348,
662   2000.
663   Smith, J. M., Bryant, M. A., and Wamsley, T. V.: Wetland buffers: numerical modeling of wave dissipation
664   by vegetation, Earth Surf. Process. Landforms, 41, 847–854, https://doi.org/10.1002/esp.3904, 2016.
665   Tang, X. and Lin, P.: Numerical and experimental studies of turbulence in vegetated open-channel flows,
666   Environmental Fluid Mechanics, 2021.
667   van Veelen, T. J., Fairchild, T. P., Reeve, D. E., and Karunarathna, H.: Experimental study on vegetation
668   flexibility as control parameter for wave damping and velocity structure, Coastal Engineering, 157,
669   103648, https://doi.org/10.1016/j.coastaleng.2020.103648, 2020.
670   Vuik, V., Jonkman, S. N., Borsje, B. W., and Suzuki, T.: Nature-based flood protection: The efficiency of
671   vegetated foreshores for reducing wave loads on coastal dikes, Coastal Engineering, 116, 42–56,
672   https://doi.org/10.1016/j.coastaleng.2016.06.001, 2016.
673   Whittaker, P., Wilson, C., Aberle, J., Rauch, H. P., and Xavier, P.: A drag force model to incorporate the
674   reconfiguration of full-scale riparian trees under hydrodynamic loading, Journal of Hydraulic Research,
675   51, 569–580, https://doi.org/10.1080/00221686.2013.822936, 2013.
676   Xu, Y. and Nepf, H.: Measured and predicted turbulent kinetic energy in flow through emergent vegetation
677   with real plant morphology, Water Resour. Res., 56, https://doi.org/10.1029/2020WR027892, 2020.

678 Yin, Z., Wang, Y., Liu, Y., and Zou, W.: Wave attenuation by rigid emergent vegetation under combined
679   wave   and   current   flows,   Ocean   Engineering,   213,   107632,
680   https://doi.org/10.1016/j.oceaneng.2020.107632, 2020.
681 Ysebaert, T., Yang, S., Zhang, L., He, Q., Bouma, T. J., and Herman, P. M. J.: Wave attenuation by two
682   contrasting ecosystem engineering salt marsh macrophytes in the intertidal pioneer zone, Wetlands,
683   31, 1043–1054, https://doi.org/10.1007/s13157-011-0240-1, 2011.
684 Zeller, R. B., Zarama, F. J., Weitzman, J. S., and Koseff, J. R.: A simple and practical model for combined
685   wave-current canopy flows, J. Fluid Mech., 767, 842–880, https://doi.org/10.1017/jfm.2015.59, 2015.
686 Zhang, X. and Nepf, H.: Flow-induced reconfiguration of aquatic plants, including the impact of leaf
687   sheltering, Limnology and Oceanography, 65, 2697–2712, https://doi.org/org/10.1002/lno.11542,
688   2020.
689 Zhang, X., Lin, P., Gong, Z., Li, B., and Chen, X.: Wave attenuation by Spartina alterniflora under macro-
690   tidal and storm surge conditions, Wetlands, 40, 2151–2162, https://doi.org/10.1007/s13157-020-
691   01346-w, 2020.
692 Zhang, X. and Nepf, H.: Wave damping by flexible marsh plants influenced by current, Phys. Rev. Fluids,
693   6, 100502, https://doi.org/10.1103/PhysRevFluids.6.100502, 2021a.
694 Zhang, X. and Nepf, H.: Wave-induced reconfiguration of and drag on marsh plants, Journal of Fluids and
695   Structures, 100, 103192, https://doi.org/10.1016/j.jfluidstructs.2020.103192, 2021b.
696 Zhang, X., Lin, P., and Nepf, H.: A simple wave damping model for flexible marsh plants, Limnology and
697   Oceanography, 66, 4182–4196, https://doi.org/doi: 10.1002/lno.11952, 2021.
698 Zhang, X., Lin, P., and Nepf, H.: A wave damping model for flexible marsh plants with leaves considering
699   linear   to   weakly   nonlinear   wave   conditions,   Coastal   Engineering,   175,   104124,
700   https://doi.org/10.1016/j.coastaleng.2022.104124, 2022.
701 Zhang, X. and Nepf, H.: Reconfiguration of and drag on marsh plants in combined waves and current,
702   Journal of Fluids and Structures, 110, 103539, https://doi.org/10.1016/j.jfluidstructs.2022.103539,
703   2022.
704 Zhang, X. and Nepf, H.: A dataset on the hydrodynamic force on individual salt marsh plants and the flow
705   structure and wave dissipation over a meadow of plants under waves with and without current. figshare.
706   Dataset. https://doi.org/10.6084/m9.figshare.24117144.v2, 2023a
707 Zhang, X. and Nepf, H.: Salt marsh dynamic motion videos under waves with and without current. figshare.
708   Media. https://doi.org/10.6084/m9.figshare.24117324.v1, 2023b.
709 Zhao, C., Tang, J., and Shen, Y.: Experimental study on solitary wave attenuation by emerged vegetation
710   in currents, Ocean Engineering, 220, 108414, https://doi.org/10.1016/j.oceaneng.2020.108414, 2020.
711 Zhu, L., Zou, Q., Huguenard, K., and Fredriksson, D. W.: Mechanisms for the asymmetric motion of
712   submerged aquatic vegetation in waves: A consistent-mass cable model, J. Geophys. Res. Oceans, 125,
713   e2019JC015517, https://doi.org/10.1029/2019JC015517, 2020.
714